IEEE Access
Multidisciplinary ⋮ Rapid Review ⋮ Open Access Journal

Received 15 November 2022, accepted 2 December 2022, date of publication 9 December 2022,
date of current version 15 December 2022.

Digital Object Identifier 10.1109/ACCESS.2022.3228111

RESEARCH ARTICLE

In-Depth Study of the Corona Discharge Breakdown Thresholds in Groove Gap Waveguides and Enhancement Strategies for Inductive Bandpass Filters

AITOR MORALES-HERNÁNDEZ[1], (Member, IEEE), MIGUEL ÁNGEL SÁNCHEZ-SORIANO[1], (Senior Member, IEEE), MIGUEL FERRANDO-ROCHER[1], (Member, IEEE), STEPHAN MARINI[1], (Senior Member, IEEE), AND VICENTE E. BORIA[2], (Fellow, IEEE)

[1]Department of Physics, Systems Engineering and Signal Theory, University of Alicante, 03690 Alicante, Spain
[2]iTEAM, Universitat Politècnica de València, 46022 Valencia, Spain

Corresponding author: Aitor Morales-Hernández (aitor.morales@ua.es)

This work was supported in part by the Fellowship Grant through the University of Alicante under Grant UAFPU2018-054, and in part by the Sub-Projects C41 and C43 of the Coordinated Project PID2019-103982RB through the Ministerio de Ciencia e Innovación (Spanish Government) under Grant MCIN/AEI/10.13039/501100011033.

ABSTRACT This work focuses on the study of the corona discharge breakdown in groove gap waveguides (GGWs) and inductive bandpass filters (BPFs) based on this technology. With the main aim of improving the peak power handling capability (PPHC), the location of the maximum normalized electric field strength ($|\hat{E}_{MAX}|$) as a function of the geometrical parameters is analyzed. First, the research deals with wave-guiding structures, comparing the distribution of the transverse electric TE_{10}-like mode of a GGW to that of an equivalent rectangular waveguide (RW). Next, a design strategy based on the adjustment of the geometrical dimensions of the bed of nails is proposed, thus achieving a considerable reduction of $|\hat{E}_{MAX}|$. The second part of this paper aims for vertically polarized GGW BPFs, where the inductive irises become the most critical part of the component. By a simple modification of their dimensions, a second design criterion is suggested for improving the PPHC. Finally, several Ku-band BPFs centered at 14 GHz and 16 GHz have been manufactured and experimentally verified at the European High-Power Radiofrequency Space Laboratory. This measurement campaign shows peak power thresholds up to 1.09 kW and 3.59 kW at 600 mbar for the non- and full-optimized GGW BPFs, respectively, thereby demonstrating a PPHC enhancement up to 5.16 dB in the high-pressure range when both strategies, proposed in this work, are used.

INDEX TERMS Corona breakdown, gas discharge, groove gap waveguides, microwave bandpass filters, peak power handling capability (PPHC), power applications, voltage magnification.

I. INTRODUCTION

Radiofrequency (RF) front-ends operating at microwave and millimeter wave (mm-wave) frequencies are formed, as it is commonly known, of different devices that process the incoming signal at the output stage of the transmitter from the intermediate-radiofrequency (IF-RF) converter to the antenna. Among all the components that are present at this stage of any ground and satellite communication system [1], [2] (e.g., RF amplifiers, mixers, oscillators, or diplexers), filters are one of the most fundamental and frequently investigated components in the literature [3], [4]. In this way,

The associate editor coordinating the review of this manuscript and approving it for publication was Photos Vryonides.

a great effort is being made by the scientific community in developing high-performance filters and, especially, as it will be shown in this work, in the advancement of high-power filters to fulfill the ever-increasing RF power requirements.

From the designer's point of view, and related to the physical phenomena that may limit the power handling capability (PHC) in RF filters [5] (or other microwave components), it is necessary to keep in mind the thermal effects [6], passive intermodulation (PIM) [7], multipactor breakdown [8], [9], [10] and corona discharge [11], [12], [13]. The latter, also commonly known as corona effect or gas breakdown, occurs if the surrounding gas molecules are ionized when the strength of the electric field is high enough. It can appear when high peak-to-average power ratio (PAPR) signals are applied to the devices, so it is important to study this physical effect and propose solutions to improve the peak power handling capability (PPHC) in microwave components, especially those working on the RF transmitting front-ends. In particular, it is worth noting that narrowband filters are very susceptible to the corona effect because a high voltage/electric field magnification takes place in the resonators [6], which confirms the relevance of its study.

Several technologies can be used for the practical implementation of filtering solutions depending on the requirements of the particular application, such as those based on planar (e.g., stripline, microstrip, or substrate integrated waveguide), coaxial or waveguide technologies [3], [4]. The selection of one of them will depend on the different properties, advantages and drawbacks of each technological solution. When high-power is not a requirement, planar technology can be appropriate due to its compact size, low weight and ease of the manufacturing process. On the other hand, waveguide technology can be the most suitable solution for high-power applications, despite its greater weight and size compared to the previous one.

In the development of microwave and mm-wave filters, one of the most relevant and novel alternatives to rectangular waveguides (RWs) is the gap waveguide (GW) technology, first introduced in [14]. It is well known that the main benefit of GWs is the possibility to avoid the problems that can appear when the contact is not perfect between the different metal layers (e.g., the possible appearance of electromagnetic leakage, PIM, and/or the decrease of the PHC), which is particularly important at high frequencies due to the miniaturization of the components and their difficulty of assembly. Moreover, other advantages are also introduced, such as the reduction of mechanical complexity and fabrication costs. GW is mainly characterized by two metallic parallel plates, where one of them is a high impedance surface (HIS) made of a periodic and metallic bed of short-circuited nails, whereas the second one introduces a perfect electric conductor (PEC) boundary condition. The combination of both metal plates hinders the propagation of the electromagnetic (EM) fields through the GW structure over a certain frequency range. Moreover, this bandstop behavior can be centered and adjusted to the desired frequency and bandwidth by modifying the main geometrical dimensions of the pins [15]. If some of these nails are removed, it is possible to achieve a wave-guiding structure where a transverse electric TE_{10}-like mode (similar to the TE_{10} mode of a conventional RW) is propagated [16], thereby obtaining the so-called groove gap waveguide (GGW) technology [17]. Furthermore, it is possible to achieve the propagation of a quasi-transverse electromagnetic (TEM) mode by using other different GW versions, such as ridge (RGW) [18] or microstrip (MGW) [19].

At this point, it is important to note that, due to the high flexibility and advantages previously introduced by the GW technology, several microwave components can be found in the literature where this type of structure is used. One of the broadest applications of GWs is the design of mm-wave antenna systems [20]. Moreover, other components have also been developed by multiple researchers around the world, such as phase shifters [21], power dividers [22], couplers [23], diplexers [24], or waveguide twists [25], among others. The characteristic pin pattern can also be a good alternative for circuit packaging to avoid leakage problems [26].

As previously stated, filters are fundamental components in any communication system. In particular, and based on the GGW technology, several topologies of bandpass filters (BPFs) can be found in the literature. By way of illustration, a filter with coaxial cavities operating in the Ka-band is presented in [27]. Moreover, other examples of BPFs based on capacitive irises [28] or carved realizations [29] have been proposed, as well as narrowband filters with high-Q resonators, manufacturing flexibility and no sidewalls are studied in [30]. It is also important to note that the GGW technology can also be an effective way for the design of multilayer filters [31], or even for implementing horizontally polarized cavity filters [32]. However, probably the most common and easiest way for implementing vertically polarized filters is based on the use of inductive irises as inter-cavity and input/output couplings [33], [34].

Regarding the importance of studying the peak power limits that microwave devices can withstand, some works have focused their efforts on studying the gas breakdown in RWs [35], [36], [37]. Some other contributions have analyzed this same physical effect in planar devices [6], [38] and several design solutions have been proposed to enhance the PPHC [39], [40], [41]. With respect to previous research related to the corona discharge breakdown thresholds in GW technology, a preliminary study based on simulations for guided structures can be found in [42], where measured results are not presented. Moreover, a strategy for enhancing the PPHC in horizontally polarized BPFs has been proposed in [43], where a measured improvement of 8.7 dB in the high-pressure range has been demonstrated. Also, other recent trends can be highlighted in the area of the corona discharge breakdown in microwaves, such as those where some novel numerical approaches have been studied [44], [45].

The manuscript contents of this work are organized as follows. In Section II, the corona discharge breakdown will

be studied for GGWs, and the distribution of the TE_{10}-like mode will be analyzed to identify the critical zones where the electric field strength is maximum. Then, a strategy for enhancing PPHC in these guided structures will be proposed. In Section III, the study will be focused on vertically polarized GGW BPFs, where practical guidelines about the design of the inductive irises of the filters will also be provided to achieve higher peak power thresholds. In Section IV, the analysis results obtained in the previous sections will be validated by testing several BPFs at the European High-Power RF Space Laboratory. Finally, the main conclusions of this work will be summarized in Section V.

Finally, and based on the introduced above, the major contributions of this work can be listed as follows:

- The variation of the electric field strength, which may limit the corona discharge breakdown thresholds, has been analyzed as a function of the frequency and size of the bed of nails of a generic GGW structure.
- Due to de lack of any previous design strategy for improving the peak power thresholds in wave-guiding GGW structures, the adjustment of the three main geometrical dimensions of the pins is here proposed to decrease the maximum electric field strength. Consequently, the same PPHC as that of a conventional RW (considered as the best-case outcome) is achieved.
- A similar parametric analysis is also carried out for the design of high-PPHC vertically polarized GGW BPFs, thus suggesting a second novel criterion based on the modification of the dimensions of the irises.
- A measurement campaign validates all the preliminary simulated results, thereby demonstrating the feasibility of both proposed design strategies.
- In this sense, they could be considered an effective way for the industry and the microwave community to develop high-power GGW components that work in ground and satellite communication systems.

II. ANALYSIS OF CORONA DISCHARGE BREAKDOWN IN GROOVE GAP WAVEGUIDES

As previously stated, it is quite evident the relevance of studying the corona discharge breakdown thresholds in microwave components that work at the output stages of the RF front-ends. As one may expect, this is the only way to ensure the development of high-PPHC devices that can satisfy the increasingly strict RF power requirements.

In particular, the PPHC of GGWs has been hardly addressed in the literature, and just with simulated results [42]. Therefore, an in-depth analysis is carried out in this section to study the variation of the maximum electric field strength (which limits the peak power thresholds) in waveguides where the groove gap technology is used. In this sense, the TE_{10}-like mode of a GGW (named from this moment as TE_{10}^{GGW}) is compared to the conventional TE_{10} mode of an equivalent RW (called as TE_{10}^{RW}), whose electric

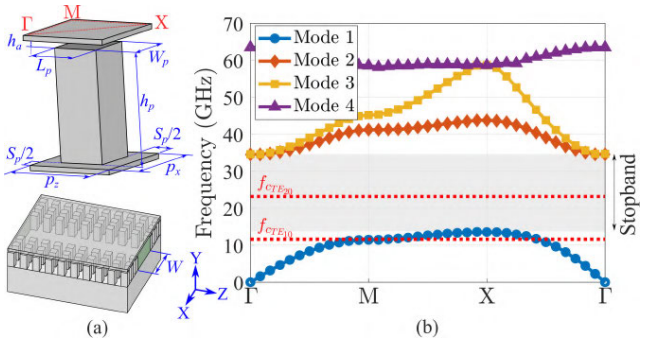

FIGURE 1. (a) Layouts of a pin unit cell and a generic GGW structure. (b) Dispersion diagram when $h_p = 3.80$ mm, $h_a = 0.20$ mm, $W_p = L_p = 1.88$ mm and $S_p = 1.34$ mm. The cutoff frequencies of the TE_{10} and TE_{20} modes of a standard WR-51 RW are also specified by using horizontal dotted red lines.

field in the vertical direction is expressed as

$$E_{TE_{10}^{RW}} = E_y(x) = E_{MAX} \cdot \cos\left(\frac{\pi x}{W_{RW}}\right) \cdot e^{-j\beta z} \qquad (1)$$

where E_{MAX} is the maximum electric field strength, W_{RW} is the width of the RW, β is the propagation constant of the fundamental mode, and the origin of the X-axis is located in the center of the waveguide cross-section.

Moreover, the maximum electric field strength of the GGW is analyzed in terms of the frequency and the main parameters of the bed of nails. Finally, a design strategy is proposed based on an optimization of the geometrical dimensions of the pins for enhancing the PPHC in GGWs.

A. STUDY OF THE TE_{10}^{GGW}-LIKE MODE AND THE VARIATION OF THE MAXIMUM ELECTRIC FIELD STRENGTH

As it is commonly known, the main geometrical dimensions of the pins that compose the bed of nails of a generic GGW structure are the height (h_p), width (W_p), length (L_p), periodicity (p_x and p_z) and the air gap (h_a), as shown in Fig. 1(a). Note that the periodicity can also be modeled by the separation between pins (S_p) as $p_x = W_p + S_p$ and $p_z = L_p + S_p$. Depending on the values of these parameters, it is possible to adjust the stopband behavior of the structure, thus forbidding the propagation of the EM fields through the bed of nails in a desired range of frequencies. By way of illustration, in Fig. 1(b), one can also see the dispersion diagram for fixed values of $h_p = 3.80$ mm, $h_a = 0.20$ mm, $W_p = L_p = 1.88$ mm and $S_p = 1.34$ mm, where a bandgap between 13.59 GHz and 34.26 GHz is achieved, completely covering the Ku- and K-bands, and most of the Ka-band. It has been simulated by using the eigenmode solver of the commercial software tool ANSYS High-Frequency Structure Simulator (HFSS).

Next, if some pins of the bed of nails are removed, a TE_{10}^{GGW}-like mode can be propagated through a guided structure of width W, as also shown in Fig. 1(a). Please, note at this point that the rest of the results that will be shown in

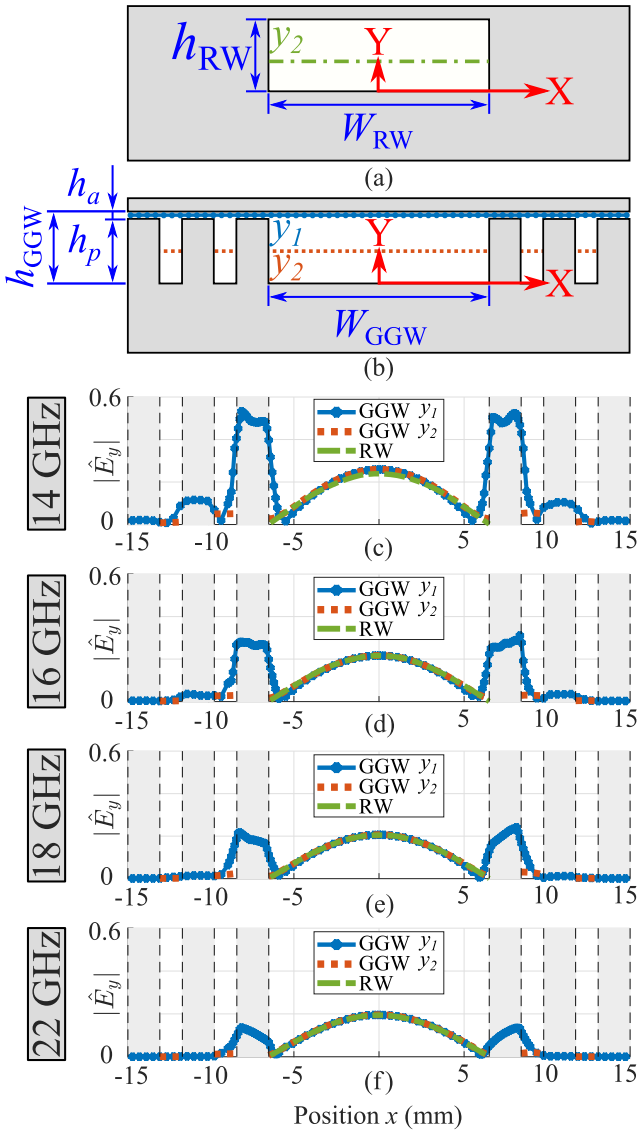

FIGURE 2. $|\hat{E}_y(x)|$ at different frequencies and two height planes. All curves have been normalized with respect to a common value of 3.0e4 V/m (when an excitation signal of 1 W is applied in simulations). Front view of the (a) RW and the (b) GGW. Normalized electric field distribution at (c) 14 GHz, (d) 16 GHz, (e) 18 GHz, and (f) 22 GHz.

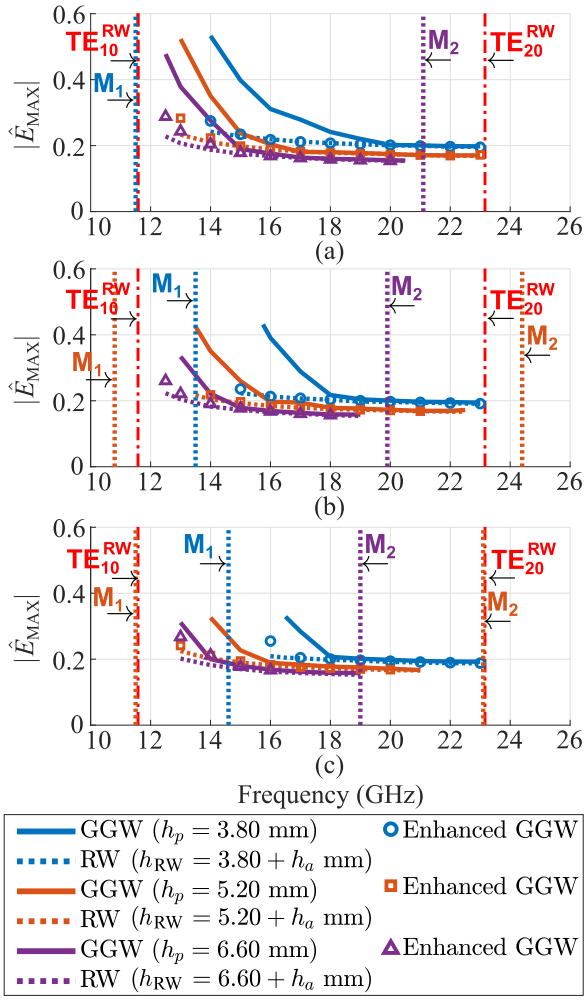

FIGURE 3. Comparison of $|\hat{E}_{MAX}|$ for different frequencies and dimensions h_p and h_a of the pins. All cases have been normalized with respect to a common value of 3.0e4 V/m. Solid lines represent $|\hat{E}_{MAX}|$ in GGWs, whereas dotted lines are used for the counterpart RWs. Vertical dashed red lines indicate the cutoff frequencies $f_{c_{TE_{10}}}$ and $f_{c_{TE_{20}}}$ of a standard WR-51, whereas vertical dotted lines (M_1 and M_2) represent the stopband region of each GGW. The unplotted lines M_1 and M_2 mean they are out of band between 10 GHz and 26 GHz. The discrete circles, squares and triangles symbolize the improved $|\hat{E}_{MAX}|$ of a GGW with the application of the design strategy described in Section II-B. (a) $h_a =$ 0.20 mm. (b) $h_a =$ 0.40 mm. (c) $h_a =$ 0.60 mm.

this work will be particularized to a standard width WR-51 (where $W = 12.954$ mm). It is also important to mention that the geometrical dimensions of the pins previously specified have been intentionally selected in order to force the beginning of the stopband region to a similar frequency to that of the first propagation mode of a standard WR-51 (i.e., $f_{c_{TE_{10}}} = 11.57$ GHz, as represented in Fig. 1(b) by using a horizontal dotted red line).

In Fig. 2, according to the same study and results presented in [16] and [42], the differences between the first propagation mode of a GGW and the counterpart RW can be observed, by means of the variation of the normalized electric field strength in the plane X-Y ($|\hat{E}_y|$), whose values have also been obtained by using ANSYS HFSS. Note that the established equivalences of the widths and heights of both simulated structures are $W_{RW} = W_{GGW} = W$ and $h_{RW} = h_{GGW} = h_p + h_a$, respectively. One can also see that each graph in Figs. 2(c)−(f) represents a different frequency in the range of operation specified above (i.e., 14 GHz, 16 GHz, 18 GHz, and 22 GHz). Furthermore, as also detailed in Figs. 2(a) and (b), $|\hat{E}_y(x)|$ is simulated at two different heights. The first plane is located in the middle of the air gap (i.e., $y_1 = h_p + h_a/2$, plotted by a solid blue line) and the second plane is placed in the middle of the pin's height (i.e., $y_2 = h_p/2$, where a dotted red line and a dashed green line are used for the GGW and the RW designs, respectively).

On the one hand, it is easy to observe that the TE_{10}^{GGW}-like mode is mostly confined and has a similar shape to that of

the TE_{10}^{RW} at higher frequencies (closer to the upper stopband limit), where the maximum $|\hat{E}_y|$ is located in the center of the waveguide propagation section, see by way of illustration Fig 2(f). On the other hand, when the operating frequency is close to the lower cut-off frequency of the stopband region, a high electric field strength is concentrated in the air gap above the first lateral row of pins, as shown in Fig. 2(c) by the appearance of two secondary lobes at height y_1. In addition, the $|\hat{E}_y|$ at the center of the propagation section of the GGW may also be slightly higher than that expected for the equivalent RW. Therefore, in this second case, one can anticipate that the corona discharge breakdown can occur in the air gap above the first lateral row of pins, due to the appearance of the secondary lobes of high $|\hat{E}_y|$. Consequently, the PPHC in a GGW may be decreased at these frequencies close to the lower stopband limit compared to the peak power thresholds of a conventional RW.

In this way, an additional study has been carried out to extend the previous analysis to other frequencies and dimensions of the pins. For this purpose, several layouts of a generic GGW as shown in Fig.1(a) have been designed and simulated for all the possible combinations of $h_p = \{3.80, 5.20, 6.60\}$ mm and $h_a = \{0.20, 0.40, 0.60\}$ mm. Note that the rest of the dimensions are set to the same values as in the preceding study (i.e., $S_p = 1.34$ mm, $W_p = L_p = 1.88$ mm, and $W = 12.954$ mm). Moreover, the counterpart RWs have also been computed to make a comparison between both technologies. In Fig. 3, the maximum normalized electric field strength ($|\hat{E}_{MAX}|$) has been plotted for each case. Note that each graph is used for a fixed value of h_a, whereas each color represents a different value of h_p (as specified in the legend), which affects the height of the propagation section (i.e., h_{RW} and h_{GGW}). It is worth mentioning that all values have been measured at the middle of the air gap (i.e., at height y_1) to avoid singularities at the sharp edges of the pins' top.

It is easy to observe that the same conclusions obtained in the previous study are extended to other configurations of h_p and h_a. On the one hand, $|\hat{E}_{MAX}|$ in a GGW is similar to that expected in a RW at frequencies close to the upper stopband limit. On the other hand, if the operating frequency is located in the lower part of the stopband, the appearance of secondary lobes in the air gap above the first lateral row of pins leads to a considerable increase in the electric field strength with respect to the equivalent RW, as previously seen. Moreover, it is also possible to check that the increase in the propagation section's height (h_{GGW} or h_{RW}) results, as expected, in a decrease of $|\hat{E}_{MAX}|$ for both technologies and a shift of the GGW's stopband region to a lower frequency range if h_p is increased.

Based on the foregoing, one may think that a high concentration of the electric field strength above the pins may significantly limit the PPHC of waveguides where the groove gap technology is used. Moreover, this effect is considered more relevant for lower values of h_p and h_a, as shown in Fig. 3. In this sense, it becomes necessary to propose a design criterion to achieve a TE_{10}^{GGW}-like mode as similar as possible to the TE_{10}^{RW}. By doing that, it will be possible to enhance the PPHC in GGWs by the reduction of $|\hat{E}_{MAX}|$ at the lateral pins and, consequently, its displacement to the center of the waveguide propagation section.

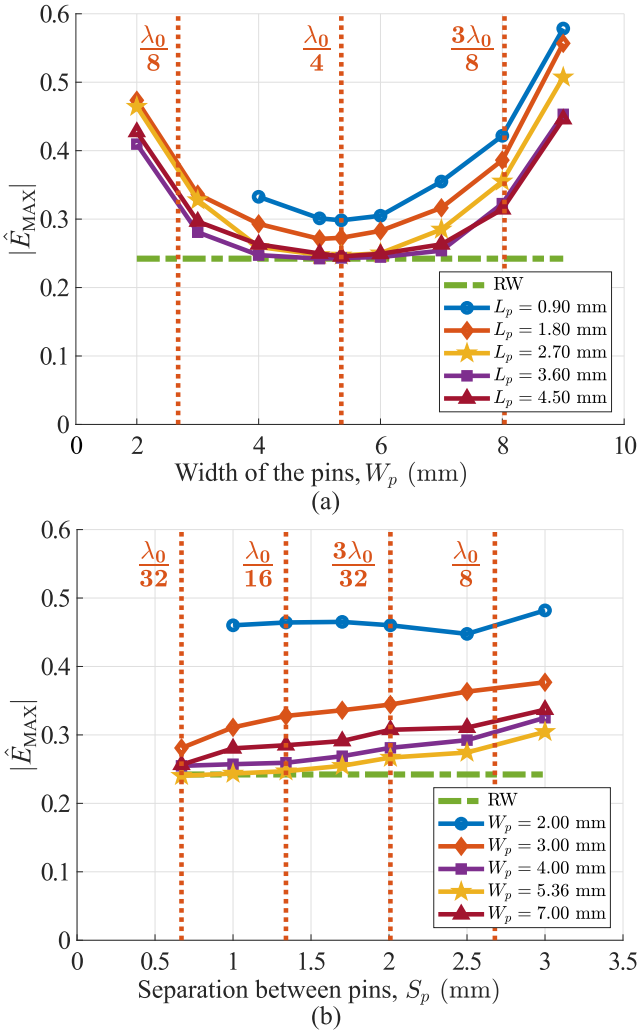

FIGURE 4. Variation of $|\hat{E}_{MAX}|$ at 14 GHz as a function of the width, length and separation between pins for $h_p = 3.80$ mm and $h_a = 0.20$ mm. All values have been normalized with respect to a common value of 3.0e4 V/m. A dashed horizontal green line is used for representing $|\hat{E}_{MAX}|$ of the equivalent RW. (a) Study of W_p and L_p. (b) Study of S_p.

B. STRATEGY FOR ENHANCING CORONA DISCHARGE BREAKDOWN IN GROOVE GAP WAVEGUIDES

In view of the above results, a strategy for improving PPHC in GGWs is described in this section. It is based on the optimization of three geometrical dimensions of the pins in order to decrease $|\hat{E}_{MAX}|$ and achieve a more confined TE_{10}^{GGW}-like mode. The three parameters to adjust are the width (W_p), length (L_p) and separation (S_p) between pins.

In Fig. 4(a), the variation of the maximum normalized electric field as a function of the width and

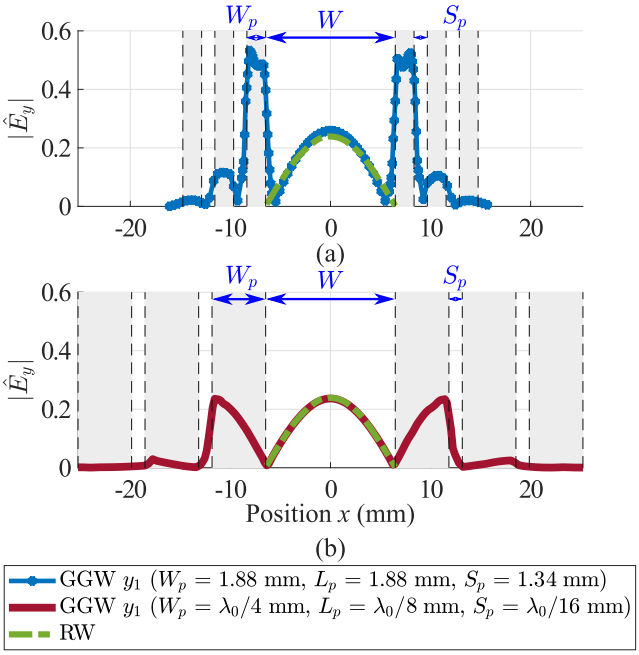

FIGURE 5. Variation of $|\hat{E}_y(x)|$ at 14 GHz. (a) Original design. (b) Optimized design with the proposed strategy to decrease $|\hat{E}_{MAX}|$.

length of the pins is represented. In order to obtain these results, different groove gap waveguides have been simulated for all the possible combinations of $W_p = \{2.00, 3.00, 4.00, 5.00, 5.36, 6.00, 7.00, 8.00, 9.00\}$ mm and $L_p = \{0.90, 1.80, 2.70, 3.60, 4.50\}$ mm, and where the separation has been set to $S_p = 1.34$ mm. At this point, it is important to highlight that the analysis is focused on the critical frequency $f_0 = 14$ GHz because, as shown in Fig. 2(c), the electric field strength of the secondary lobes, in this case, is higher than at the other frequencies. Moreover, the height of the pins and the air gap have also been fixed to $h_p = 3.8$ mm and $h_a = 0.2$ mm, respectively, because this combination is one of the worst cases shown in Fig. 3 (i.e., there is a greater difference in the maximum electric field strength between the GGW and the equivalent RW). It is easy to observe in Fig. 4(a) that $|\hat{E}_{MAX}|$ in the GGW is similar to the counterpart RW when $W_p = 5.36$ mm $\approx \lambda_0/4$ and $L_p \geq 2.70$ mm $\approx \lambda_0/8$. Therefore, one can expect that assuming these optimized dimensions as a first-order approximation, the achieved peak power thresholds of both technologies will also be similar.

Next, the separation between pins has also been studied. For this analysis, the length of the pins has been fixed to a value of $L_p = 2.70$ mm $\approx \lambda_0/8$ based on the previous results, whereas several combinations of $S_p = \{0.67, 1.00, 1.34, 1.70, 2.00, 2.50, 3.00\}$ mm and $W_p = \{2.00, 3.00, 4.00, 5.36, 7.00\}$ mm have been simulated, and their maximum normalized electric field strengths have been plotted in Fig. 4(b). In this case, it is observed that the influence of S_p on the $|\hat{E}_{MAX}|$ variation is the lowest one compared to W_p and L_p. Moreover, it is important to note that a very narrow separation between pins is not possible since the beginning of the stopband behavior is shifted to a frequency higher than $f_0 = 14$ GHz and, for this reason, these values of S_p are not included in the representation. On the other hand, the EM fields are less confined, $|\hat{E}_{MAX}|$ is higher and the return losses are decreased for values of $S_p \geq 3$ mm, as it has also been verified. In this sense, a good compromise for achieving a similar value of $|\hat{E}_{MAX}|$ between the GGW and the equivalent RW may be $S_p = 1.34$ mm $\approx \lambda_0/16$, as shown in Fig. 4(b).

Finally, it is necessary to extend the proposed design strategy for improving PPHC in GGWs to other frequencies and configurations of the bed of nails, due to the fact that the previous study has only been carried out for a particular case. In this way, the enhanced maximum normalized electric field strength when applying the suggested design criterion is also represented in Fig. 3 by using discrete points (i.e., blue circles for $h_p = 3.80$ mm, red squares for $h_p = 5.20$ mm and purple triangles for $h_p = 6.00$ mm). It is easy to observe that $|\hat{E}_{MAX}|$ of the enhanced GGWs is significantly decreased, achieving similar values to those simulated for the equivalent RWs. Therefore, one can expect that after the proposed adjustment of parameters W_p, L_p and S_p, the PPHC of a groove gap waveguide will be considerably improved. However, it is important to note at this point that, as it has also been verified, the bandwidth of the stopband region will be slightly reduced by the application of the proposed pins' geometrical dimensions. In this sense, the use of the design strategy is specially useful when the operating frequency is close to the lower stopband limit, whereas, for higher frequencies, the margin of enhancement will be limited. Thus, the expected PPHC improvement will be achieved due to the modification of the stopband behavior when the proposed design criterion is applied, which contributes to the reduction of the secondary lobes above the first lateral row of pins. One can see this effect in Fig. 5, where a comparison between the TE_{10}^{GGW}-like mode of the original and the optimized designs (plotted in blue and brown color, respectively) is represented.

III. ANALYSIS OF CORONA DISCHARGE BREAKDOWN IN GGW INDUCTIVE BANDPASS FILTERS

In this section, the technique used for decreasing the maximum electric field strength in guided structures using groove gap technology is applied to evaluate the same effect in narrowband inductive GGW bandpass filters. A parametric analysis is presented to obtain a design strategy for the dimensions of the inductive irises (in the same way as it has been done before for the geometrical dimensions of the lateral pins), since, as it will be shown next, the maximum electric field strength of a GGW BPF is mainly concentrated in the air gap above the irises.

At this point, it is also worth noting that the GGW filters that will be shown in what follows will also be useful to demonstrate the conclusions obtained in the previous Section II. In this sense, the approximate power breakdown thresholds of the preceding GGW structures can be

TABLE 1. Main dimensions of the manufactured BPFs.

Prototype	Tech.	f_0 (GHz)	W_p (mm)	L_p (mm)	S_p (mm)	W_{ir} (mm)	L_{ir} (mm)	$W_{c1} = W_{c4}$ (mm)	$W_{c2} = W_{c3}$ (mm)	$L_1 = L_3$ (mm)	L_2 (mm)
Benchmark	RW	14	—	—	—	—	5.36	9.02	6.96	14.13	15.91
[B]	GGW	14	1.88	1.88	2.27	1.88	1.88	9.04	7.31	16.72	18.27
[C]	GGW	14	1.88	1.88	2.27	4.02	5.36	9.48	7.82	14.53	16.24
[D]	GGW	14	5.36	2.68	1.34	4.02	5.36	9.43	7.69	13.11	14.80
[E]	GGW	16	1.88	1.88	2.27	3.52	4.69	8.16	6.65	9.88	10.97

analytically computed as

$$P_{\text{break}} = \frac{|E_{\text{break,air}}|^2}{|E_{\text{MAX}}|^2} \tag{2}$$

where $|E_{\text{break,air}}|$ is the air dielectric breakdown at a particular pressure ($\sim$ MV/m in the high-pressure range), and $|E_{\text{MAX}}|$ is the maximum electric field strength (without normalization) in the previous GGW structures when an excitation signal of 1 W is applied, and whose values can be obtained from Fig. 3. In this way, the expected power breakdown limit of the GGW designs presented in Section II may be of several tens of kilowatts, which are very high power levels to be provided by an amplifier in a laboratory testbed. The design of GGW BPFs allows us to reach lower peak values than those in guided structures and, therefore, they will be more feasible to measure. The main reason for this fact is that a voltage/electric field magnification occurs in the resonant cavities, so higher values of $|E_{\text{MAX}}|$ than in guided structures are achieved. This leads to lower values of P_{break}, as shown in equation (2).

The study presented in this section is focused on third-order vertically polarized GGW bandpass filters (VP-GGW BPFs). Please, note that all the prototypes that will be simulated in the following analysis are designed with a center frequency $f_0 = 14$ GHz and a passband bandwidth of 140 MHz (fractional bandwidth FBW = 1%). Moreover, these filters have an ideal Chebyshev response with 20 dB return loss and, as previously stated, the inter-cavity and input/output couplings have been implemented by using inductive irises. Please, note that the main reason for centering the designs at the Ku-band (even though the GGW technology makes more sense at higher frequencies) was mainly conditioned by the limitations of the measurement campaign's testbed described in the following Section IV, which was limited for frequencies between 10.5 GHz and 18.5 GHz. The height of the waveguide propagation section is fixed in all cases at $h_{\text{RW}} = h_{\text{GGW}} = 4$ mm, where the pin's height and the air gap in the GGW BPFs are $h_p = 3.80$ mm and $h_a = 0.20$ mm, respectively. This decision has been made to force the appearance of secondary lobes at 14 GHz since, as mentioned above, the GGW BPFs presented in this section will also be useful to assess the appearance of secondary lobes at the lateral pins of the resonant cavities when the operating frequency is close to the lower stopband limit, as explained in more detail in the preceding Section II.

First, a conventional third-order RW bandpass filter (called benchmark) has been designed, as shown in Fig. 6(a),

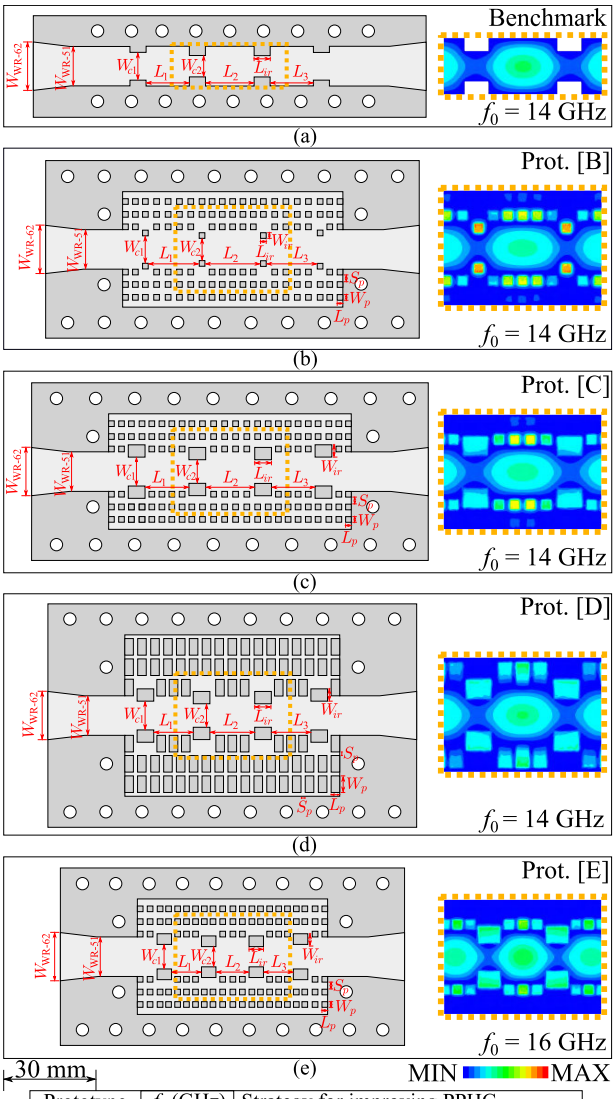

Prototype	f_0 (GHz)	Strategy for improving PPHC
Benchmark	14	RW
[B]	14	GGW - Non-optimized
[C]	14	GGW - Semi-optimized (only irises)
[D]	14	GGW - Full-optimized (irises and pins)
[E]	16	GGW - Semi-optimized (only irises)

(f)

FIGURE 6. Filters' top view and electric field distribution of the second resonant cavity (the same scale is applied in all cases). (a) Benchmark. (b) Filter B. (c) Filter C. (d) Filter D. (e) Filter E. (f) Summary table of the strategy used for improving the PPHC of each manufactured BPF.

to compare its maximum electric field strength with the GGW filters. Note that a transition from WR-62 to WR-51 has also been included at the input and output ports because

this modification will be necessary for the measurement campaign described in the following Section IV. Next, a VP-GGW BPF (called filter B) has also been designed, where the dimensions of the inductive irises are the same as those of the lateral pins (i.e., $W_{ir} = W_p$ and $L_{ir} = L_p$, as shown in Fig. 6(b) and also detailed in Table 1). Note that the pins located just behind the irises have been removed to avoid a very narrow separation between them. In Fig. 6, the electric field distribution at the second resonant cavity (whose voltage magnification is the highest at f_0 [6]) is also plotted on the plane located in the middle of the air gap (i.e., at height $y_1 = h_p + h_a/2$, as in the previous analysis described in Section II). One can observe that a high concentration of the electric field is located above the irises of filter B whereas, in the benchmark prototype, it is placed at the center of the resonant cavity with lower strength. Furthermore, it is also important to emphasize that $|\hat{E}_{\mathrm{MAX}}|$ above the irises of filter B is higher than above the lateral pins of the cavities. Based on the foregoing, and from the point of view of maximizing the PPHC, it can be expected that the irises are the critical part of the VP-GGW BPF. Therefore, it is necessary to find optimal dimensions for the design of the coupling windows in order to shift the maximum electric field strength to another part of the filter (preferably to the center of the cavity, as in the benchmark prototype). In this sense, and in a similar way as previously done for W_p, L_p and S_p, the variation of $|\hat{E}_{\mathrm{MAX}}|$ as a function of the parameters W_{ir} and L_{ir} will be analyzed in the following subsection.

A. STRATEGY FOR ENHANCING CORONA DISCHARGE BREAKDOWN IN GGW INDUCTIVE BANDPASS FILTERS

For this study, different VP-GGW BPFs based on inductive irises have been simulated for all the possible combinations of $W_{ir} = \{2.00, 3.00, 4.00, 5.00, 6.00, 7.00, 8.00\}$ mm and $L_{ir} = \{2.00, 3.00, 4.00, 5.00, 5.36, 6.00, 7.00, 8.00\}$ mm, where the dimensions of all the inter-cavity and input/output irises of the filter have been modified in the same way. Please, note that in order to avoid the appearance of $|\hat{E}_{\mathrm{MAX}}|$ in the air gap above the lateral pins of the resonant cavities, the optimized dimensions of W_p, L_p and S_p previously presented in Section II have been set in all the simulations. The obtained results are shown in Fig. 7, where the maximum electric field strength is represented as a function of L_{ir}, and various colors are used to represent different values of W_{ir}. On the one hand, it is easy to see that all curves show the same trends and reach convergence for values of $L_{ir} \geq 5.36$ mm $\approx \lambda_0/4$. On the other hand, the parameter W_{ir} has more influence than the length of the irises since, as it can be observed, $|\hat{E}_{\mathrm{MAX}}|$ in the VP-GGW BPF is similar to those of the counterpart RW filter when $4.0\,\mathrm{mm} \leq W_{ir} \leq 6.0\,\mathrm{mm}$ (i.e., $0.75 \cdot L_{ir} \leq W_{ir} \leq 1.25 \cdot L_{ir}$). In this sense, one can assume these values of W_{ir} and L_{ir} as a first-order approximation of the irises' design criterion for maximizing the PPHC in VP-GGW BPFs.

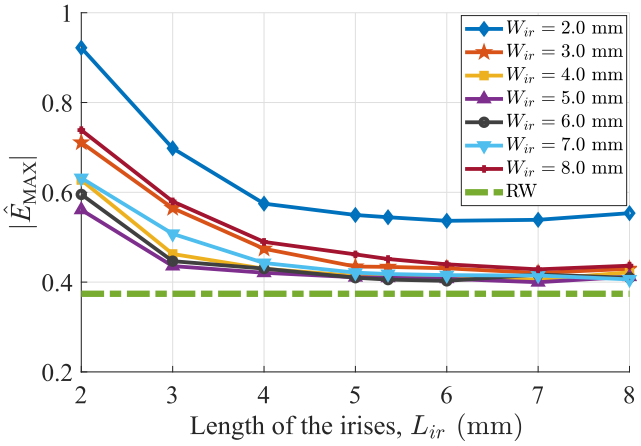

FIGURE 7. Variation of $|\hat{E}_{\mathrm{MAX}}|$ at 14 GHz as a function of W_{ir} and L_{ir}. All values have been normalized with respect to a common value of 9.0e4 V/m. A dashed horizontal green line is used for representing the equivalent RW.

B. RESULTS

Finally, to evaluate the previous conclusions, three additional third-order bandpass filters have been simulated. First, a semi-optimized VP-GGW BPF (called filter C) has been designed. For this case, only the dimensions of the irises have been optimized, whereas the dimensions of the lateral pins have not been modified with respect to filter B, as shown in Fig. 6(c). Furthermore, a full-optimized VP-GGW BPF (called filter D) has also been designed, where both previous strategies for improving PPHC (i.e., lateral pins and irises) have been applied, as represented in Fig. 6(d). Finally, an additional prototype (called filter E) has been designed at $f_0 = 16$ GHz with a fractional bandwidth of 1% and a Chebyshev response with 20 dB return loss, whose layout is represented in Fig. 6(e). As one can observe, the latter prototype is similar to filter C, where the only difference lies in the modification of the main parameters to adjust f_0 at 16 GHz (which also affects the optimized dimensions W_{ir} and L_{ir}, whereas W_p, L_p and S_p are the same as in filter C). Filter E will be useful in Section IV to demonstrate the decrease of the secondary lobes above the first lateral row of pins at higher frequencies, as one can also easily see by the comparison of the electric field distributions between Figs. 6(c) and (e) (and as previously explained in more detail in Section II). Please, note that the main dimensions of all the BPFs described above are also summarized in Table 1, whereas the strategy used for improving PPHC in each case is detailed in Fig. 6(f).

By way of illustration, and to better understand the variation of the maximum electric field strength by modifying the width/length of the lateral pins and the inductive irises, a comparison between filters B, C and D is shown in Fig. 8. First, in Fig. 8(a) the filter B is represented, where one can see that $|\hat{E}_{\mathrm{MAX}}|$ is located in the air gap above the irises, whereas lower electric field strength is concentrated over the lateral pins of the resonant cavity, as previously stated. Next, if the design criterion for optimizing W_{ir} and L_{ir} is applied

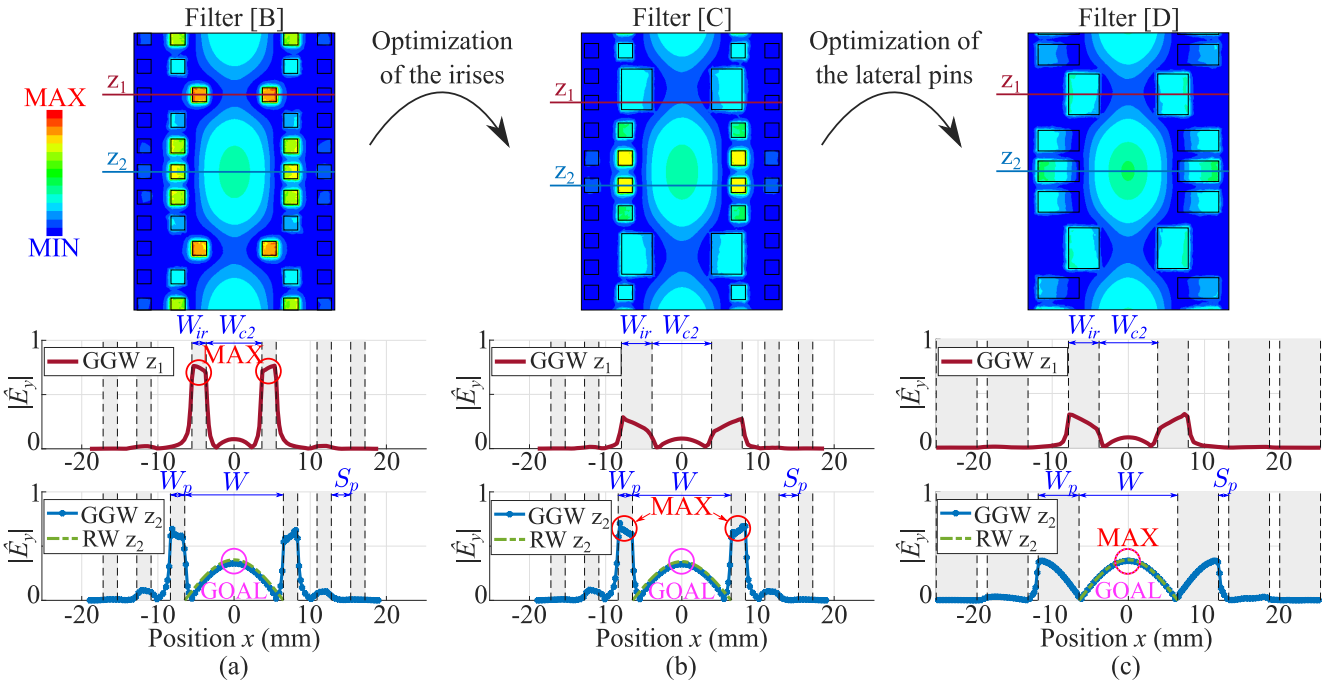

FIGURE 8. Variation of $|\hat{E}_y(x)|$ at $f_0 =$ 14 GHz for three different VP-GGW BPFs. The electric field strength of the second resonant cavity is plotted in the middle of the air gap (i.e., $y_1 = h_p + h_a/2$) and the same scale is applied in all cases. $|\hat{E}_y(x)|$ in plane z_1 (above the irises) and plane z_2 (above the lateral pins) are also plotted in two different graphs by using brown and blue colors, respectively. Red circles are used for highlighting the zones where the electric field strength is maximum in each case, whereas the pink circles mark the desired $|\hat{E}_{MAX}|$ goal. A dashed green line represents $|\hat{E}_y(x)|$ of the counterpart RW BPF. All graphs have been normalized with respect to a common value of 9.0e4 V/m. (a) Filter B. (b) Filter C. (c) Filter D.

(whereas W_p, L_p and S_p remain identical to those of filter B), the filter C is obtained, as shown in Fig 8(b). In this case, it is easy to observe that the electric field strength over the irises is considerably decreased and, consequently, $|\hat{E}_{\mathrm{MAX}}|$ is now shifted to the air gap above the lateral pins of the cavity. However, the electric field strength is still too high compared to the desired $|\hat{E}_{\mathrm{MAX}}|$ goal value of the equivalent RW BPF. For that reason, the last step is represented in Fig. 8(c), where the design strategy proposed in Section II-B is also applied to the lateral pins of the resonant cavities. In this way, the filter D is obtained, where the maximum electric field strength is now shifted to the center of the resonant cavity, and reduced to the same value as the counterpart RW BPF. Therefore, one can easily see in Fig. 8 that, by a simple adjustment of the main dimensions of the pins that compose the bed of nails and, especially, the inductive irises of a VP-GGW BPF, the maximum electric field strength can be equated to that of an equivalent RW filter, thus confirming the results obtained in both parametric studies described in the previous Sections II-B and III-A. Consequently, a considerable improvement of the PPHC with respect to the original/non-optimized design (filter B) will be expected, as it will be shown in what follows.

IV. IMPLEMENTATION AND EXPERIMENTAL RESULTS

In view of the above results, it has been demonstrated that by a simple modification of the main geometrical dimensions of the bed of nails (W_p, L_p and S_p) and the inductive irises

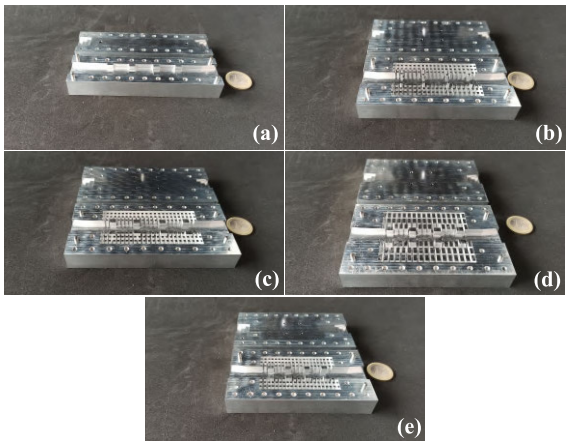

FIGURE 9. Manufactured prototypes. (a) Benchmark. (b) Filter B. (c) Filter C. (d) Filter D. (e) Filter E.

(W_{ir} and L_{ir}), one can easily enhance the PPHC of a VP-GGW BPF. This improvement can be achieved by the reduction of the maximum electric field strength, and its concentration at the center of the waveguide propagation section. Thus, in the following paragraphs, the previous conclusions will be demonstrated by means of experimental measurements. In order to obtain the peak power thresholds that each BPF summarized in Table 1 can reach, all the proposed prototypes shown in Fig. 6 have been manufactured in aluminum, as shown in Fig. 9, by using a computer numerical control (CNC) Datron M25 milling machine.

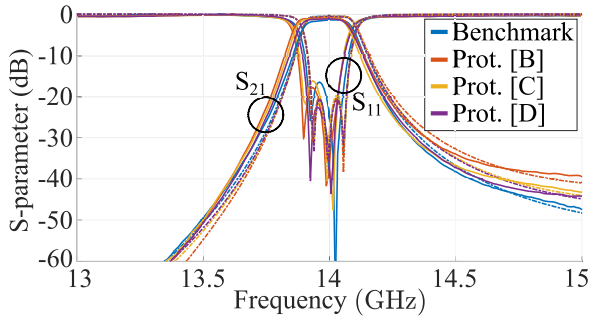

FIGURE 10. Simulated (dashed lines) and measured (solid lines) S-parameters of all filters centered at 14 GHz.

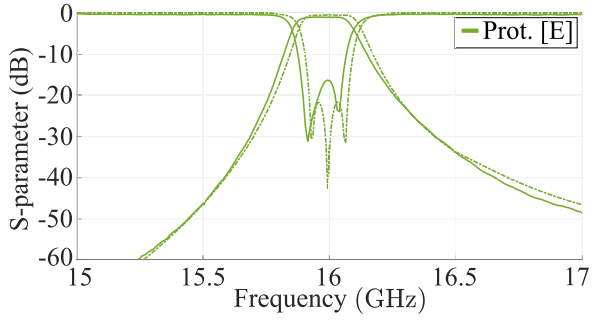

FIGURE 11. Simulated (dashed line) and measured (solid line) S-parameters of the filter centered at 16 GHz.

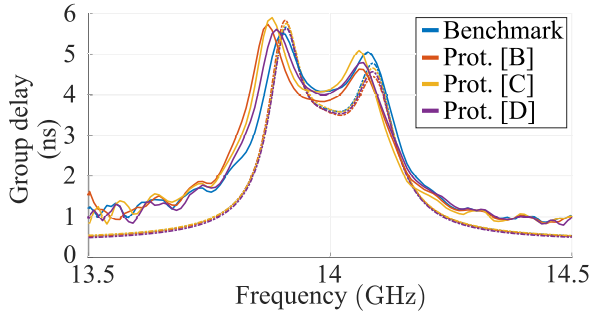

FIGURE 12. Simulated (dashed lines) and measured (solid lines) group delay of all filters centered at 14 GHz.

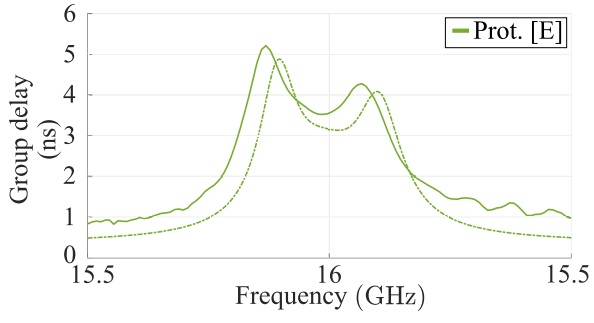

FIGURE 13. Simulated (dashed line) and measured (solid line) group delay of the filter centered at 16 GHz.

After the manufacturing process, the S-parameter responses have been measured and represented in Figs. 10 and 11.

TABLE 2. Measured characteristics of the manufactured prototypes.

Prototype	Tech.	f_0 (GHz)	FBW (%)	IL (dB)	RL (dB)
Benchmark	RW	13.99	0.964	1.30	16.4
[B]	GGW	13.96	1.021	0.83	17.7
[C]	GGW	13.97	0.986	0.99	16.1
[D]	GGW	13.97	0.957	1.07	22.5
[E]	GGW	15.97	0.944	0.99	16.3

TABLE 3. Measured PPHC enhancement (with respect to filter B).

Pressure	115 (mbar)	275 (mbar)	400 (mbar)	600 (mbar)
RW Benchmark	1.21 dB	3.55 dB	4.22 dB	5.26 dB
[D]	0.76 dB	3.37 dB	4.02 dB	5.16 dB

Furthermore, the group delay has also been measured for all prototypes, as shown in Figs. 12 and 13. As one can clearly see, all the measurements have a high level of similarity with the counterpart full-wave simulations. In addition, the measured center frequency (f_0), fractional bandwidth (FBW) and insertion/return losses (IL/RL) of each manufactured prototype are summarized in Table 2.

On the one hand, only a slight shift of f_0 to a lower frequency and a small variation of the FBW can be highlighted in both technologies (i.e., RW and GGW). On the other hand, it is important to note that the return losses are in all cases better than 16.1 dB. Finally, as also shown in Fig. 10, the upper rejection band can be considerably improved with respect to the non-optimized prototype (filter B) when the dimensions of the inductive irises (filter C) and also of the lateral pins (filter D) are adjusted to the dimensions previously studied in Sections II and III.

All the prototypes have been tested in a measurement campaign performed at the European High Power RF Space Laboratory (located in Valencia, Spain). In Fig. 14, the generic scheme of the testbed configuration used for the corona breakdown detection is shown. The measurements have been carried out at two different frequencies which correspond to the measured center frequency of each prototype: 13.98 GHz (for filters A, B, C and D) and 15.97 GHz (for filter E). Moreover, a pulsed signal with a low duty cycle (2 %) and low width (20 μs) has been used to avoid any self-heating effect in the devices under test (DUTs). Please, note that the maximum applied signal power of the testbed is 4 kW, and all filters have been measured at 22 °C in a pressure-controlled chamber from 2 to 1013 mbar to obtain their respective Paschen curves. Five different methods have been used for the corona discharge detection: nulling of the forward/reverse power at the operation frequency, third-harmonic detection, a broadband diode, an electron avalanche monitoring, and an optical detection system. When two or more of these methods were detected, the corona discharge breakdown was considered to have occurred.

In Fig. 15, the measured peak power thresholds of the manufactured prototypes working at $f_0 = 14$ GHz are represented.

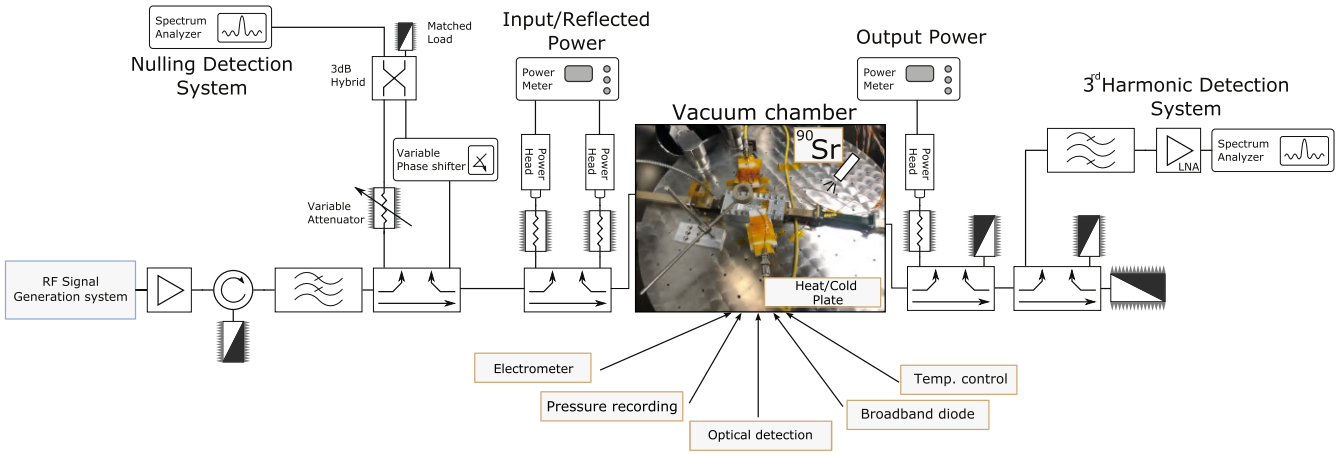

FIGURE 14. Scheme of the testbed configuration used for corona breakdown detection.

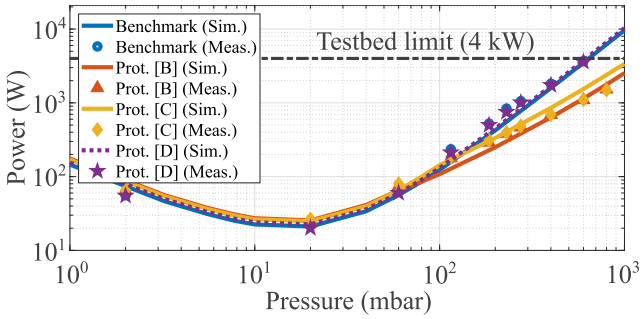

FIGURE 15. Simulated and measured corona discharge thresholds (Paschen curves) of the prototypes working at $f_0 = 14$ GHz.

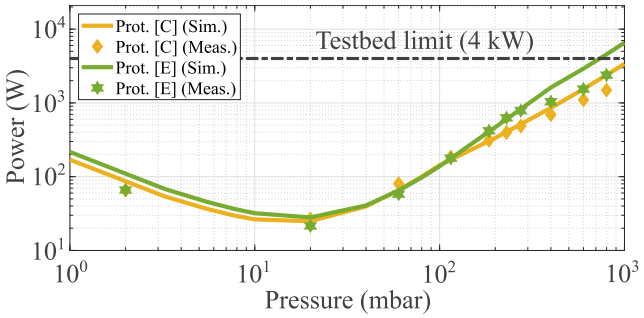

FIGURE 16. Simulated and measured corona discharge thresholds (Paschen curves) of filter E (working at $f_0 = 16$ GHz) for comparison with the counterpart values of filter C (working at $f_0 = 14$ GHz).

Note that the corresponding simulated values obtained using the software tool SPARK3D [46], which solves the diffusion type problem for the evolution of the electron density, are also included. First, the PPHC of the RW BPF (benchmark) is plotted in blue color, which represents the maximum peak power limit that the equivalent GGW BPFs can reach. Next, it can be observed that the appearance of the gas breakdown in the non-optimized filter B (represented in red color) leads to lower values of peak power thresholds, especially in the high-pressure range (above 200 mbar). If the geometrical dimensions of the pins of the inductive irises (W_{ir} and L_{ir}) are optimized (obtaining the filter C, which is plotted in yellow color), the maximum electric field strength is shifted to the air gap above the lateral pins of the resonant cavities, so the PPHC is still maintained similar to that of the previous prototype. However, if the dimensions of the bed of nails (W_p, L_p and S_p) are also adjusted, the full-optimized filter D (shown in purple color) is obtained, which achieves almost the same peak power thresholds as the RW benchmark. The main reason is that, as previously stated, the maximum electric field strength is decreased and shifted to the center of the resonant cavity. In this way, a PPHC improvement up to 5.16 dB at 600 mbar for the filter D, with respect to filter B, has been demonstrated (i.e., a PPHC up to 3.59 kW and 1.09 kW, respectively, at this pressure), as summarized, along with other pressures, in Table 3. Finally, it is also important to emphasize that the reduction of the secondary lobes at higher frequencies in the stopband region has also been verified in the measurement campaign since, as shown in Fig. 16, the filter E (centered at 16 GHz) achieves higher peak power thresholds than the filter C (centered at 14 GHz).

V. CONCLUSION

In this paper, an in-depth analysis of the variation of the electric field strength in GGW BPFs based on inductive irises has been carried out, and a simple way for improving their peak power thresholds has been presented. First, the study has been focused on wave-guiding structures, where the distribution of the TE_{10}^{GGW}-like mode has been compared to the counterpart TE_{10}^{RW} mode. As observed, secondary lobes with high electric field strength appear in the air gap above the first lateral row of pins when the operating frequency is close to the stopband lower limit, so a parametric analysis has been carried out to reduce them. When the width, length and separation of the pins that compose the bed of nails are $W_p = \lambda_0/4$, $L_p = \lambda_0/8$ and $S_p = \lambda_0/16$, respectively, a considerable reduction of $|\hat{E}_{MAX}|$ has been demonstrated.

The second study has been performed in VP-GGW BPFs working at 14 GHz, showing that the critical part is now located above the pins which define the inductive irises. In this sense, another parametric analysis has been presented to find their optimized dimensions of the length ($L_{ir} \geq \lambda_0/4$) and width ($0.75 \cdot L_{ir} \leq W_{ir} \leq 1.25 \cdot L_{ir}$) to reduce $|\hat{E}_{\mathrm{MAX}}|$ above them. Finally, the feasibility of both strategies has been validated in a measurement campaign, thereby showing how a simple adjustment of the pins can indeed lead to a considerable PPHC improvement up to 5.16 dB with respect to a non-optimized prototype. Future work will be directed to the study of other physical phenomena and technologies used for the design of microwave filtering solutions.

ACKNOWLEDGMENT

The authors would like to thank the European Space Agency (ESA) and Val Space Consortium (VSC)—Laboratories funded by the European Regional Development Fund—A Way of Making Europe, and the Antennas and Propagation Laboratory [Instituto de Telecomunicaciones y Aplicaciones Multimedia (APL—iTEAM UPV)].

REFERENCES

[1] R. E. Collin, *Foundations for Microwave Engineering*, 2nd ed. Hoboken, NJ, USA: Wiley, 2001.
[2] D. M. Pozar, *Microwave Engineering*, 4th ed. Hoboken, NJ, USA: Wiley, 2012.
[3] J.-S. Hong, *Microstrip Filters for RF/Microwave Applications*. Hoboken, NJ, USA: Wiley, 2011.
[4] R. J. Cameron, C. M. Kudsia, and R. R. Mansour, *Microwave Filters for Communication Systems*, 2nd ed. Somerset, U.K.: Wiley, 2018.
[5] M. Yu, "Power-handling capability for RF filters," *IEEE Microw. Mag.*, vol. 8, no. 5, pp. 88–97, Oct. 2007.
[6] M. A. Sánchez-Soriano, Y. Quéré, V. Le Saux, S. Marini, M. S. Reglero, V. E. Boria, and C. Quendo, "Peak and average power handling capability of microstrip filters," *IEEE Trans. Microw. Theory Techn.*, vol. 67, no. 8, pp. 3436–3448, Aug. 2019.
[7] D. Smacchia, P. Soto, V. E. Boria, and D. Raboso, "A new model to determine passive intermodulation terms when non-contributing carriers are added to classical scenarios," *IEEE Access*, vol. 9, pp. 152070–152074, 2021.
[8] J. R. M. Vaughan, "Multipactor," *IEEE Trans. Electron Devices*, vol. ED-35, no. 7, pp. 1172–1180, Jul. 1988.
[9] J. J. Vague, I. Asensio, Á. Coves, Á. A. S. Blas, M. Reglero, A. V. Pantaleoni, D. Raboso, M. Baquero-Escudero, and V. E. Boria, "Study of the multipactor effect in groove gap waveguide technology," *IEEE Trans. Microw. Theory Techn.*, vol. 70, no. 5, pp. 2566–2578, May 2022.
[10] C. Bachiller, V. Nova, A. Ferrer, and V. E. B. Esbert, "Space qualification of metalized additive manufactured filters," *IEEE Access*, vol. 10, pp. 96952–96966, 2022.
[11] A. D. MacDonald, *Microwave Breakdown in Gases*. New York, NY, USA: Wiley, 1966.
[12] Y. P. Raizer, *Gas Discharge Physics*. Berlin, Germany: Springer, 1991.
[13] D. Anderson, U. Jordon, M. Lisak, T. Olsson, and M. Ahlander, "Microwave breakdown in resonators and filters," *IEEE Trans. Microw. Theory Techn.*, vol. 47, no. 12, pp. 2547–2556, Dec. 1999.
[14] P.-S. Kildal, E. Alfonso, A. Valero-Nogueira, and E. Rajo-Iglesias, "Local metamaterial-based waveguides in gaps between parallel metal plates," *IEEE Antennas Wireless Propag. Lett.*, vol. 8, pp. 84–87, 2009.
[15] E. Rajo-Iglesias and P.-S. Kildal, "Numerical studies of bandwidth of parallel-plate cut-off realised by a bed of nails, corrugations and mushroom-type electromagnetic bandgap for use in gap waveguides," *IET Microw., Antennas Propag.*, vol. 5, no. 3, pp. 282–289, Feb. 2011.
[16] A. Berenguer, V. Fusco, D. E. Zelenchuk, D. Sánchez-Escuderos, M. Baquero-Escudero, and V. E. Boria-Esbert, "Propagation characteristics of groove gap waveguide below and above cutoff," *IEEE Trans. Microw. Theory Techn.*, vol. 64, no. 1, pp. 27–36, Jan. 2016.
[17] M. Ferrando-Rocher, A. Valero-Nogueira, J. I. Herranz-Herruzo, A. Berenguer, and B. Bernardo-Clemente, "Groove gap waveguides: A contactless solution for multilayer slotted-waveguide array antenna assembly," in *Proc. 10th Eur. Conf. Antennas Propag. (EuCAP)*, Apr. 2016, pp. 1–4.
[18] P.-S. Kildal, A. U. Zaman, E. Rajo-Iglesias, E. Alfonso, and A. Valero-Nogueira, "Design and experimental verification of ridge gap waveguide in bed of nails for parallel-plate mode suppression," *IET Microw., Antennas Propag.*, vol. 5, no. 3, pp. 262–270, Mar. 2011.
[19] H. Raza, J. Yang, P.-S. Kildal, and E. A. Alós, "Microstrip-ridge gap waveguide–Study of losses, bends, and transition to WR-15," *IEEE Trans. Microw. Theory Techn.*, vol. 62, no. 9, pp. 1943–1952, Sep. 2014.
[20] T. Zhang, R. Tang, L. Chen, S. Yang, X. Liu, and J. Yang, "Ultra-wideband full-metal planar array antenna with a combination of ridge gap waveguide and E-plane groove gap waveguide," *IEEE Trans. Antennas Propag.*, vol. 70, no. 9, pp. 8051–8058, Sep. 2022.
[21] D. Sanchez-Escuderos, J. I. Herranz-Herruzo, M. Ferrando-Rocher, and A. Valero-Nogueira, "True-time-delay mechanical phase shifter in gap waveguide technology for slotted waveguide arrays in Ka-band," *IEEE Trans. Antennas Propag.*, vol. 69, no. 5, pp. 2727–2740, May 2021.
[22] A. Farahbakhsh, D. Zarifi, and A. U. Zaman, "60-GHz groove gap waveguide based wideband H-plane power dividers and transitions: For use in high-gain slot array antenna," *IEEE Trans. Microw. Theory Techn.*, vol. 65, no. 11, pp. 4111–4121, Nov. 2017.
[23] D. Zarifi, A. Farahbakhsh, and A. U. Zaman, "Design and fabrication of wideband millimeter-wave directional couplers with different coupling factors based on gap waveguide technology," *IEEE Access*, vol. 7, pp. 88822–88829, 2019.
[24] A. Vosoogh, M. S. Sorkherizi, A. U. Zaman, J. Yang, and A. A. Kishk, "An integrated Ka-band diplexer-antenna array module based on gap waveguide technology with simple mechanical assembly and no electrical contact requirements," *IEEE Trans. Microw. Theory Techn.*, vol. 66, no. 2, pp. 962–972, Feb. 2018.
[25] D. Sun and J. Xu, "Real time rotatable waveguide twist using contactless stacked air-gapped waveguides," *IEEE Microw. Wireless Compon. Lett.*, vol. 27, no. 3, pp. 215–217, Mar. 2017.
[26] E. Rajo-Iglesias, A. U. Zaman, and P.-S. Kildal, "Parallel plate cavity mode suppression in microstrip circuit packages using a lid of nails," *IEEE Microw. Wireless Compon. Lett.*, vol. 20, no. 1, pp. 31–33, Jan. 2010.
[27] M. Baquero-Escudero, A. Valero-Nogueira, M. Ferrando-Rocher, B. Bernardo-Clemente, and V. E. Boria-Esbert, "Compact combline filter embedded in a bed of nails," *IEEE Trans. Microw. Theory Techn.*, vol. 67, no. 4, pp. 1461–1471, Apr. 2019.
[28] Z. Liu, J.-Y. Deng, and D. Sun, "Slow-wave groove gap waveguide bandpass filter," *IEEE Access*, vol. 7, pp. 52581–52588, 2019.
[29] M. Rezaee and A. U. Zaman, "Realisation of carved and iris groove gap waveguide filter and E-plane diplexer for V-band radio link application," *IET Microw., Antennas Propag.*, vol. 11, no. 15, pp. 2109–2115, Oct. 2017.
[30] A. U. Zaman, P.-S. Kildal, and A. A. Kishk, "Narrow-band microwave filter using high-Q groove gap waveguide resonators with manufacturing flexibility and no sidewalls," *IEEE Trans. Compon., Packag., Manuf. Technol.*, vol. 2, no. 11, pp. 1882–1889, Nov. 2012.
[31] T. Xiu, Y. Yao, H. Jiang, X. Cheng, C. Wang, B. Wang, J. Yu, and X. Chen, "Design of a compact and low-loss E-band filter based on multilayer groove gap waveguide," *IEEE Microw. Wireless Compon. Lett.*, vol. 31, no. 11, pp. 1211–1214, Nov. 2021.
[32] M. Rezaee and A. U. Zaman, "Groove gap waveguide filter based on horizontally polarized resonators for V-band applications," *IEEE Trans. Microw. Theory Techn.*, vol. 68, no. 7, pp. 2601–2609, Jul. 2020.
[33] E. A. Alós, A. U. Zaman, and P.-S. Kildal, "Ka-band gap waveguide coupled-resonator filter for radio link diplexer application," *IEEE Trans. Compon., Packag., Manuf. Technol.*, vol. 3, no. 5, pp. 870–879, May 2013.
[34] A. Berenguer, M. Baquero-Escudero, D. Sánchez-Escuderos, B. Bernardo-Clemente, and V. E. Boria-Esbert, "Low insertion loss 61 GHz narrow-band filter implemented with groove gap waveguides," in *Proc. 44th Eur. Microw. Conf.*, Oct. 2014, pp. 191–194.
[35] C. Ernst and V. Postoyalko, "Prediction of peak internal fields in direct-coupled-cavity filters," *IEEE Trans. Microw. Theory Techn.*, vol. 51, no. 1, pp. 64–73, Jan. 2003.

[36] C. Vicente, M. Mattes, D. Wolk, B. Mottet, H. Hartnagel, J. Mosig, and D. Raboso, "Microwave breakdown prediction in rectangular waveguide based components," in *Proc. German Microw. Conf.*, 2005, pp. 17–20.
[37] T. Pinheiro-Ortega, J. Monge, S. Marini, J. Sanz, E. Sorolla, M. Mattes, C. Vicente, J. Gil, V. E. Boria, and B. Gimeno, "Microwave corona breakdown prediction in arbitrarily-shaped waveguide based filters," *IEEE Microw. Wireless Compon. Lett.*, vol. 20, no. 4, pp. 214–216, Apr. 2010.
[38] F. J. P. Soler, S. Anza, M. Mattes, C. M. España, F. Quesada, M. Jimenez, J. Gil, C. Vicente, J. R. Mosig, D. Raboso, V. E. Boria, B. Gimeno, and A. Alvarez-Melcon, "Rigorous investigation of RF breakdown effects in high power microstrip passive circuits," in *IEEE MTT-S Int. Microw. Symp. Dig.*, Jun. 2009, pp. 833–836.
[39] A. Morales-Hernández, M. Á. Sánchez-Soriano, S. Marini, M. S. Reglero, L. Esteve, V. E. Boria, and M. Guglielmi, "Enhancement of corona discharge thresholds in microstrip bandpass filters by using cover-ended resonators," *Int. J. Microw. Wireless Technol.*, vol. 13, no. 7, pp. 708–718, Sep. 2021.
[40] A. Morales-Hernández, M. A. Sánchez-Soriano, S. Marini, V. E. Boria, and M. Guglielmi, "Increasing peak power handling in microstrip bandpass filters by using rounded-end resonators," *IEEE Microw. Wireless Compon. Lett.*, vol. 31, no. 3, pp. 237–240, Mar. 2021.
[41] A. Morales-Hernández, M. A. Sánchez-Soriano, S. Marini, V. E. Boria, and M. Guglielmi, "Cover-ended resonators to increase corona discharge thresholds in microstrip bandpass filters," in *Proc. 50th Eur. Microw. Conf. (EuMC)*, Jan. 2021, pp. 882–885.
[42] A. Morales-Hernández, M. Ferrando-Rocher, M. A. Sánchez-Soriano, S. Marini, and V. E. Boria, "Design strategy and considerations to improve corona discharge breakdown in groove gap waveguides," in *Proc. 15th Eur. Conf. Antennas Propag. (EuCAP)*, Mar. 2021, pp. 1–5.
[43] A. Morales-Hernández, M. A. Sánchez-Soriano, M. Ferrando-Rocher, S. Marini, M. T. Calduch, and V. E. Boria, "Peak power handling capability in groove gap waveguide filters based on horizontally polarized resonators and enhancement solutions," *IEEE Microw. Wireless Compon. Lett.*, vol. 32, no. 7, pp. 859–862, Jul. 2022.
[44] M. A. Abouelatta, S. A. Ward, A. M. Sayed, K. Mahmoud, M. Lehtonen, and M. M. F. Darwish, "Fast corona discharge assessment using FDM integrated with full multigrid method in HVDC transmission lines considering wind impact," *IEEE Access*, vol. 8, pp. 225872–225883, 2020.
[45] M. A. Abouelatta, S. A. Ward, A. M. Sayed, K. Mahmoud, M. Lehtonen, and M. M. F. Darwish, "Measurement and assessment of corona current density for HVDC bundle conductors by FDM integrated with full multigrid technique," *Electr. Power Syst. Res.*, vol. 199, pp. 107370-1–107370-9, Oct. 2021.
[46] *SPARK3D, Copyright 2022 Dassault Systèmes*. Accessed: 2022. [Online]. Available: https://www.3ds.com/products-services/simulia/products/spark3d/

AITOR MORALES-HERNÁNDEZ (Member, IEEE) was born in Alicante, Spain, in 1992. He received the bachelor's degree in telecommunication technologies and services engineering from the Universitat Politècnica de València (UPV), Valencia, Spain, in 2014, and the master's degree in telecommunication engineering and the Ph.D. degree in physics applied to sciences and technologies from the University of Alicante (UA), Alicante, in 2017 and 2022, respectively.

In 2019, he joined the Microwave and Applied Computational Electromagnetics Group (GMECA), Institute of Physics Applied to Science and Technologies (FACyT-UA), UA. His research interests include the study and design of microwave filtering devices, focusing on their power-handling capabilities.

Dr. Morales-Hernández was a recipient of the Extraordinary master's degree Award from UA and the Valencian Telecommunication Engineers Association (COITCV), in 2017, and the URSI Conference Best Student Paper Finalist's Recognition, in 2021.

MIGUEL ÁNGEL SÁNCHEZ-SORIANO (Senior Member, IEEE) was born in Murcia, Spain, in 1984. He received the master's degree in telecommunications engineering and the Ph.D. degree in electrical engineering from Miguel Hernandez University (UMH), Elche, Spain, in 2007 and 2012, respectively.

In 2007, he joined the Radiofrequency Systems Group, UMH, as a Research Assistant. In 2010, he was a Visiting Researcher with the Microwaves Group, Heriot-Watt University, Edinburgh, U.K. In January 2013, he joined the LabSTICC Group, Université de Bretagne Occidentale, Brest, France, as a Postdoctoral Researcher, where he worked for two years. From January 2015 to September 2015, he was a "Juan de la Cierva" Research Fellow with the Grupo de Aplicaciones de Microondas (GAM), Technical University of Valencia, Valencia, Spain. Since September 2015, he has been with the University of Alicante, Alicante, Spain, where he is currently an Associate Professor. His research interests include the analysis and design of microwave planar devices, especially filters and their reconfigurability and the multiphysics study of high-frequency devices.

Dr. Sánchez-Soriano was a recipient of the runner-up HISPASAT Award for the Best Spanish Doctoral Thesis in New Applications for Satellite Communications, awarded by the Spanish Telecommunication Engineers Association (COIT/AEIT) and of the Extraordinary Ph.D. Award from Miguel Hernández University. He serves as an Associate Editor for the journals, IEEE Transactions on Microwaves, Theory and Techniques and *IET Microwaves, Antennas & Propagation* and as a Regular Reviewer for more than 20 journals, including the IEEE Microwave and Wireless Components Letters, *IET Electronics Letters*, IEEE Access, and several IEEE international conferences. He received the special award for the master's degree.

MIGUEL FERRANDO-ROCHER (Member, IEEE) was born in Alcoy, Spain. He received the M.Sc. and Ph.D. degrees in telecommunication engineering from the Universitat Politècnica de València (UPV), Valencia, Spain, in 2012 and 2018, respectively.

In 2012, he joined the Complex Radiation Systems Team, Institut d'Electronique et des Technologies du numéRique (IETR), Rennes, France, as a Researcher, where he was involved in reflect array antennas for satellite applications in collaboration with Thales Alenia Space France (TASF) and Italy (TASI). Since 2013, he has been with the Antennas and Propagation Laboratory (APL), Polytechnic University of Valencia. In 2016, he joined the Chalmers University of Technology, Gothenburg, Sweden, as a Guest Researcher. Since September 2019, he has been an Assistant Professor with the Department of Physics, Systems Engineering and Signal Theory, University of Alicante, Alicante, Spain. His research activity is also developed with the Microwave and Applied Computational Electromagnetics Group (GMECA), Alicante. His current research interests include satellite communication (SATCOM) on-the-move, high-gain antennas and arrays, gap waveguide (GW) technology, and millimeter-wave components.

Dr. Ferrando-Rocher was a recipient of the Extraordinary Prize for Doctoral Theses from the Polytechnic University of Valencia, in 2020, the AIRBUS Defense and Space Award, in 2019, and the URSI Conference Best Student Paper Award, in 2017. Since 2022, he has been an Ambassador of the IEEE Young Professionals Program to inspire and inform future generations on a variety of technical and non-technical topics in the field of antennas and propagation.

STEPHAN MARINI (Senior Member, IEEE) received the Laurea degree in electronics engineering from the University of Perugia, Perugia, Italy, in 2001, and the Ph.D. degree in telecommunications from the Universidad Politécnica de Valencia, Valencia, Spain, in 2005.

In 2001, he joined the Departamento de Comunicaciones, Universidad Politécnica de Valencia, where he was involved in the framework of a European Union Project ''Millimeter-wave and Microwave Components Design Framework for Ground and Space Multimedia Network'' (MMCODEF). Since 2005, he has been a Lecturer with the Departamento de Física, Ingeniería de Sistemas y Teoría de la Señal, Universidad de Alicante, Alicante, Spain, where he became an Associate Professor, in 2012. In 2009, he became a fellow of the LEMA Laboratory, École Polytechnique Fédérale de Lausanne, Lausanne, Switzerland, as a Visiting Scientist, supported by the Spanish Government. Since October 2015 he has been the Director of the Microwave and Applied Computational Electromagnetics Group (GMECA), Institute of Physics Applied to Science and Technologies, University of Alicante. His current research interests include numerical methods in computer-aided techniques for the analysis and design of microwave and millimeter passive components and simulation of power effects (multipactor and corona) in passive waveguide systems.

Dr. Marini currently serves as an Associate Editor for *IET Electronics Letters* and a regular reviewer for the most relevant IEEE and IET technical journals in his areas of interest.

VICENTE E. BORIA (Fellow, IEEE) was born in Valencia, Spain, in May 1970. He received the Ingeniero de Telecomunicación (Hons.) and Doctor Ingeniero de Telecomunicación degrees from the Universidad Politécnica de Valencia, Valencia, in 1993 and 1997, respectively.

In 1993, he joined the Departamento de Comunicaciones, Universidad Politécnica de Valencia, where he has been a Full Professor, since 2003. In 1995 and 1996, he was holding a Spanish trainee position with the European Space Research and Technology Centre, European Space Agency (ESTEC-ESA), Noordwijk, The Netherlands, where he was involved in the area of EM analysis and design of passive waveguide devices. He has authored or coauthored ten chapters in technical textbooks, 180 articles in refereed international technical journals, and over 200 articles in international conference proceedings. His current research interests include the analysis and automated design of passive components, left-handed and periodic structures, and the simulation and measurement of power effects in passive waveguide systems.

Dr. Boria has been a member of the IEEE Microwave Theory and Techniques Society (IEEE MTT-S) and the IEEE Antennas and Propagation Society (IEEE AP-S), since 1992. He is also a member of the European Microwave Association (EuMA). He is also a member of the Technical Committees of the IEEE-MTT International Microwave Symposium and the European Microwave Conference. He also serves as an Editorial Board Member of the *International Journal of RF and Microwave Computer-Aided Engineering*. He has been the Chair of the 48th European Microwave Conference held in Madrid, Spain. He acts as a regular reviewer of the most relevant IEEE and IET technical journals on his areas of interest. He has been an Associate Editor of IEEE Microwave and Wireless Components Letters, from 2013 to 2018, and *IET of Electronics Letters*, from 2015 to 2018. He serves as a Subject Editor *Microwaves Journal* for *IET of Electronics Letters*.